Assessment of intra-build variations in tensile strength in electron beam powder-bed fusion Ti-6Al-4V part 1: Effects of build height

Nicholas Derimow[1]*, Alejandro Romero[2], Aldo Rubio[2], Cesar Terrazas[2], Newell Moser[1], Orion L. Kafka[1], Jake T. Benzing[1], Francisco Medina[2], Ryan Wicker[2], Nikolas Hrabe[1]

[1] *Applied Chemicals and Materials Division, National Institute of Standards and Technology, 325 Broadway, Boulder, CO 80305, USA*

[2] *W.M. Keck Center for 3D Innovation, The University of Texas at El Paso, 500 W University Ave, El Paso, TX 79968, USA*

Abstract

In this work, rectangular blocks of electron beam powder-bed fusion (PBF-EB) additively manufactured (AM) Ti-6Al-4V were built, such that a total of 68 mini-tensile test coupons could be extracted for mechanical testing over a range of build height and build plate locations. These as-built tensile test coupons were uniaxially tested to fracture and subsequently studied via scanning electron microscopy, micro X-ray computed tomography, and inert gas fusion chemical analysis to systematically study the intra-build variations in tensile properties, microstructure, porosity, and chemistry. There were no significant contributions to this variation in yield strength (YS) from build location, porosity, grain size, or crystallographic texture. A strong correlation was observed between YS and build height, where YS was observed to decrease with increasing build height, up to 35 mm. Inert gas fusion oxygen measurements reveal the same trend, suggesting that oxygen content variation as a function of build height is causing the observed YS variation. The source of the oxygen content variation is thought to be a transient source of oxygen, such as moisture in the powder and build chamber. The establishment of this oxygen variation and its correlation to tensile properties motivates and facilitates improvements to PBF-EB Ti-6Al-4V processing, including powder mixing and handling.

Keywords: Additive manufacturing, Ti-6Al-4V, Oxidation, Tensile properties, Electron beam powder-bed fusion

*Corresponding author
Email address: nicholas.derimow@nist.gov (Nicholas Derimow[1])

1. Introduction

Additive manufacturing (AM), particularly electron beam powder-bed fusion (PBF-EB), is a widely used technique for fabricating metal parts with complex geometries and for specialized applications. One of the cornerstone alloys used with this AM process is the titanium alloy, Ti-6Al-4V, due to its high strength-to-weight ratio, biocompatibility, and corrosion resistance [1]. Ti-6Al-4V is traditionally manufactured in wrought or cast forms, and the manufacturing of Ti-6Al-4V through AM processes has created new opportunities for its application into the biomedical and aerospace industries [2, 3]. However, AM presents its own set of technical challenges for maintaining structural and chemical homogeneity in order to maintain part quality that can perform at the same level of cast/wrought material. There is a need for a thorough understanding of the processing-structure-properties-performance (PSPP) relationships in AM Ti-6Al-4V, if this material is to be fully realized for applications with risk of fatigue and fracture [4]. However, the properties of AM Ti-6Al-4V can sometimes exhibit large scatter when compared across the different technologies, and may require post-processing to preserve desirable material performance [5]. With respect to PBF-EB of Ti-6Al-4V, the effect of build plate location and part size on microstructure and mechanical properties has been characterized [6], as well as the effects of energy input and build orientation [7]. That being said, mechanical properties of PBF-EB Ti-6Al-4V can be largely dictated by oxygen content [8], porosity [9], and surface roughness [10].

In order to maintain a low process cost, PBF-EB relies on the reuse of unmelted Ti-6Al-4V powder for subsequent builds [11]. Due to the high background temperature from the layer preheating commonly used in PBF-EB Ti-6Al-4V processes, unmelted powder oxidizes slightly each build, eventually leading to an oxygen content that no longer meets applicable limits in standards ASTM F3001 [12] for Grade 23 Ti and ASTM F2924 [13] for Grade 5 Ti. Tang et al. [8] show that with increased powder reuse (and therefore increased oxygen content), yield strength (YS) can increase from 834 MPa to 960 MPa when oxygen content increases from 0.08 wt.% to 0.19 wt.%. A similar increase is observed in ultimate tensile strength (UTS) from 920 MPa to 1039 MPa for the same specimens. Popov et al. [14] also observed similar trends, with YS increasing from 872 MPa to 1028 MPa for powder that had been reused 69 times, representing a 0.124 wt.% to 0.324 wt.% increase in oxygen content. In wrought Ti-6Al-4V, similar trends are observed for increased oxygen content [15], and represent a critical area of process monitoring and control for Ti alloys across most industries and technologies.

All previous work has assumed oxidation is consistent throughout a given build area, but recent work by the present authors demonstrated a build height dependence on the oxidation of unmelted Ti-6Al-4V

powders in the powder-bed during the PBF-EB process [16]. That is, powders closer to the build plate were observed to have higher oxygen content than those near the top of the powder bed. This is hypothesized to be due to the gettering nature of Ti in high-temperature environments [17], as well as the availability of a finite oxygen source that diminishes over the course of a build (e.g. moisture in powder and build chamber).

The goal of this work is to determine if the mechanical properties of PBF-EB Ti-6Al-4V is vary as a function of build height. We show that the primary source of variation is correlated to build height, rather than build plate location, and explore possible causes for the observed correlation. To accomplish this, four larger blocks were built in the corners of the build plate to span as large an area of the build plate as possible. From each block, 17 miniature (mini) tensile specimens were machined, tensile tested, and characterized for microstructure, porosity, and oxygen content. Mini tensile specimens were used to minimize the build height and total volume of material sampled in each tensile specimen gauge section, so as to optimize our ability to observe potential variations. The decision to use mini tensile specimens is supported by recent work by Shanbhag et al. [18], which concluded that large tensile specimens may not accurately yield the mechanical properties of an actual as-built component. We did not want to assume that oxygen content would be the cause of any observed variation in tensile properties, so microstructure and porosity were also characterized. For microstructure, both α-lath thickness and crystallographic texture were evaluated via scanning electron microscopy (SEM) and electron backscatter diffraction (EBSD). Porosity, both on and near the tensile fracture surface, was evaluated using fractography and micro X-ray computed tomography (μXCT). In this way, a systematic investigation of potential intra-build variations in tensile properties for PBF-EB Ti-6Al-4V was performed, and any observed variation could be attributed to oxygen content, microstructure, or porosity.

2. Method and Materials

2.1. Electron Beam Powder-bed Fusion Parameters

The PBF-EB process was carried out on an Arcam S12[1] machine with standard Ti-6Al-4V build theme and layer height of 50 μm (software version 3.2.132.14429). The powder recoater direction was side-to-side relative to the front of the machine. The feedstock powder consisted of virgin plasma-atomized Grade 23 ELI spherical Ti-6Al-4V conforming to ASTM F3001-14 [12] with a powder size distribution (PSD) ranging from

[1]Commercial names are identified in order to specify the experimental procedure adequately. Such identification is not intended to imply recommendation or endorsement by NIST nor does it imply that they are necessarily the best available for the purpose.

45 µm to 106 µm. The portion of the particle diameters less than 50 µm, 67 µm, and 100 µm correspond to 10 %, 50 %, and 90 % (D10, D50, and D90) respectively, and were measured by the manufacturer per ASTM B822-17 [19]. Four equally spaced rectangular cuboids were chosen for this study, pictured and labeled in Fig. 1a, such that they were at the corners of the build plate and were nominally 15 mm × 15 mm × 35 mm tall (Fig. 1b). The other items on the build plate were used for a different study. The bulk/average chemistry values for both the feedstock and the cuboids are presented in Table 1.

2.2. Mechanical Testing

Seventeen mini tensile specimens were extracted by wire electrical discharge machining (EDM) from each of the four as-built rectangular cuboids, and were labeled according to build height, resulting in 68 traceable mini-tensile specimens (Fig. 1c). The nominal gauge dimensions were 5.08 mm long × 2.54 mm wide × 1.5 mm thick (Fig. 1d). Quasi-static, uniaxial tensile testing, with articulated fixtures to improve alignment, was carried out at a strain rate of 1×10^{-3} s^{-1} using a physical extensometer with gauge length of 3.0 mm.

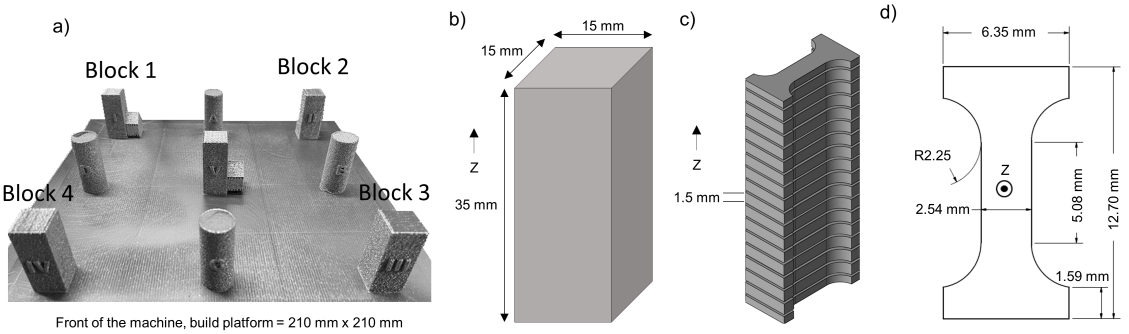

Figure 1: a) Layout of the build plate, b) As-built rectangular cuboid (not to scale) nominal dimensions, c) mini tensile specimens excised from the block, d) mini-tensile specimen machining dimensions. Z = build direction. Note, additional items on build plate (e.g. cylinders and center block) were not used in this study.

2.3. Chemistry

Bulk chemistry determination of a rectangular cuboid (with surfaces removed) was carried out as follows: Aluminum, vanadium, and iron were measured by optical emission spectroscopy (OES) per ASTM E2371-13 [20]. Oxygen and nitrogen were measured per ASTM E1409-13 [21], and hydrogen per ASTM E1447-09 [22], all by inert gas fusion. Carbon was measured by the combustion method per ASTM E1941-10 [23]. The oxygen measurements for the Block 4 specimens utilized half of each fractured Block 4 tensile specimen, including the gauge as well as grip sections. Each tensile specimen half was abraded to remove any leftover wire EDM recast layer and broken into smaller chunks to fit into the inert gas fusion specimen holder.

Virgin powder feedstock chemistry is reported directly from the manufacturer certification sheet. The bulk chemistry values for both feedstock and built material are presented in Table 1.

Table 1: Chemical composition in weight % of the ASTM F3001-14 [12] (Grade 23) limits, the virgin powder feedstock, and the built material for this work prior to machining. Feedstock chemistry is reported directly from the powder certification sheet from the manufacturer.

Elem.	F3001-14	Feedstock	Bulk
Al	5.5<x<6.5	6.39	6.00
V	3.5<x<4.5	3.93	3.99
Fe	0.25	0.20	0.19
O	0.13	0.080	0.081
C	0.080	0.010	0.014
N	0.050	0.020	0.030
H	0.0120	0.0020	0.0016
Ti	bal.	bal.	bal.

2.4. Surface and Internal Porosity

The fractured surfaces of the mechanical test specimens were imaged with light via stereoscopic microscopy. Micro X-ray computed tomography (μXCT) [24, 25] was utilized for volumetric data of the surface features and interior pores. Representative low and high yield strength post-test tensile specimens were measured with μXCT. For these experiments, an μXCT machine was utilized, and the X-ray source and detector distances were chosen such that the specified voxel edge length was 1.5 μm/voxel ± 0.03 μm/voxel. A filter was used to reduce low-energy X-rays which cause beam hardening artifacts. The X-ray source power and detector exposure time were optimized on a per-specimen basis to minimize scan time while ensuring high quality reconstructions.

The specimen was rotated 360° about its long axis, during which time 3201 X-ray radiographs were captured. The reconstructed data were then saved as an image sequence (also commonly referred to as a TIFF stack) comprising 990 image-slices. Each resultant grayscale (16-bit) image-slice was 984 pixels × 1009 pixels. The grayscale images were then binarized using global thresholding techniques and quantitative image processing methods were applied to measure the porosity.

2.5. Microstructural Characterization

The fractured pieces of the tensile specimens were mounted flat in phenolic resin such that the XY plane was observable (perpendicular to the build direction, Z). The specimens were metallographically prepared via standard abrading and polishing down to 1 μm using diamond suspension. The specimens were then vibratory polished for approximately 24 h in 0.05 μm colloidal silica. The microstructure was imaged using a field emission scanning electron microscope (FE-SEM) equipped with an annular backscatter detector for

backscatter electron (BSE) imaging. Crystallographic information was obtained using a with an electron backscatter diffraction (EBSD) detector operated at an accelerating voltage of 20 kV and EBSD step size of 1.5 µm.

3. Results

3.1. Mechanical Properties

A summary of the yield strength (YS), ultimate tensile strength (UTS), total elongation (in %), and elastic modulus is presented for all four blocks in Fig. 2. The median values for each block are identified as black bars. A scatter plot of the UTS and elongation data is presented in Fig. 3 with the dotted vertical/horizontal lines representing the minimum values for UTS and elongation as per the ASTM F2924-14 [13] standard. The points are color-coded by block. At first glance, the scatter between the UTS and elongation values follow no discernible trends, with an overall total range ($\text{Range}_{\text{UTS}}$) of UTS scatter for the entire build equal to 64.7 MPa.

We also investigated the tensile properties in the Z direction. Fig. 4 shows tensile data as a function of build height (Z) for all four blocks. This data represents the per-block variation of properties as a function of build height. The same color scheme representing tests from each block is used as in the previous scatter plots. Linear regressions are shown as dotted colored lines through the data sets, all of which show the same general trend of YS and UTS decreasing with increasing build height. There is no observable build location variation because all blocks show the same general trend as well as magnitude and range of YS/UTS values as a function of build height. The R^2 values for the linear regressions are presented next to the data legends. The $\text{Range}_{\text{YS}} = 74.2$ MPa is added to the plot to show the total range of YS values for the entire build corresponds to a difference of 8.3 % between the specimen with the lowest YS (859.3 MPa) and highest YS (933.6 MPa). The UTS can be seen to have a similar downward trend to the YS with respect to build height, however no trends are noted for the total elongation or elastic modulus. Linear regressions are presented for all four plots, however only the YS and UTS have high confidence, whereas the linear regressions for elongation and modulus show no dependence no build height.

3.2. Porosity

In order to screen for defects that may or may not have contributed to the tensile behavior, fractography was carried out on the fractured surfaces of low (859.3 MPa), medium (898.5 MPa), and high YS specimens

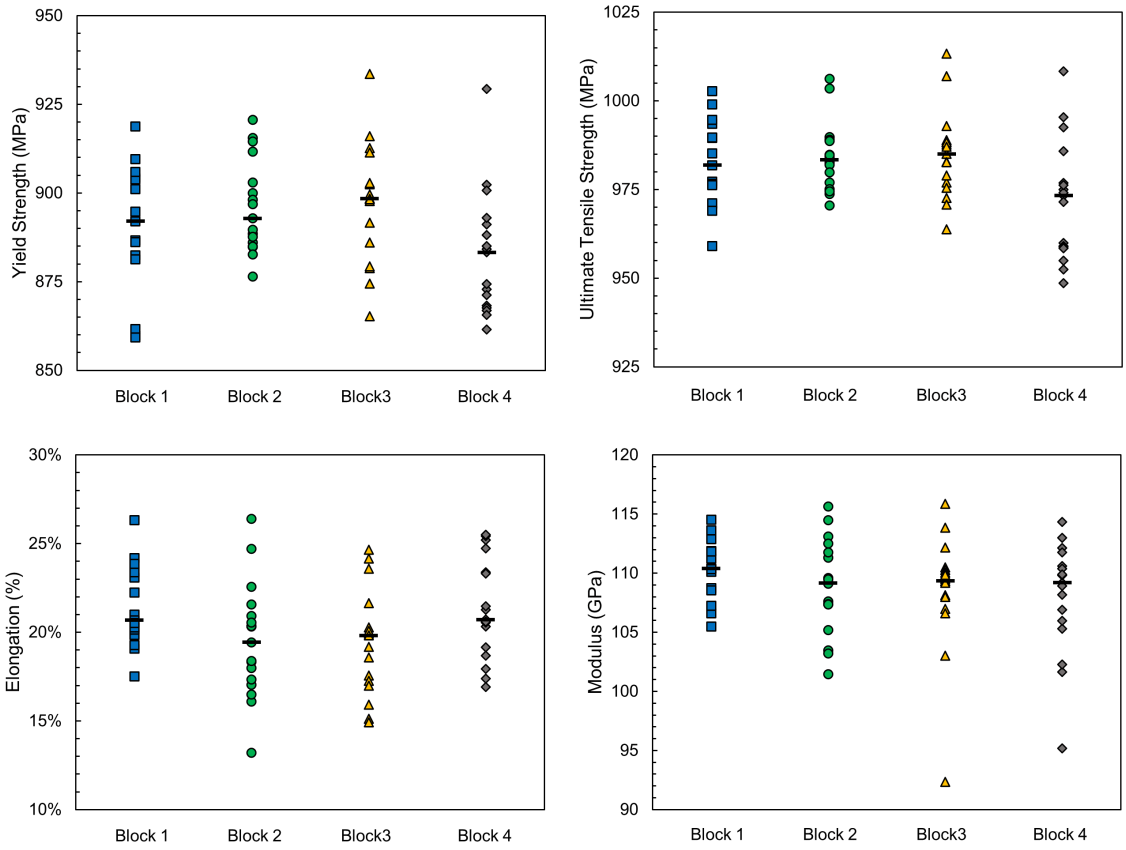

Figure 2: Summary of tensile properties for the four blocks tested in this work. Median values for each property are presented as black horizontal bars for yield strength, ultimate tensile strength, elongation at failure, and elastic modulus.

(933.6 MPa), pictured in Fig. 5a–c. The images in Fig. 5 have been flattened to show the entire fracture surface in focus. The black arrows indicate small surfaces pores present.

Fig. 6 displays the μXCT projections of the gauge section near fracture of two low YS samples from Block 1 with heights (H) corresponding to approximately 33 mm and YS = 859.0 MPa (Fig. 6a) and H ≈ 27 mm and YS = 861.6 MPa (Fig. 6b). There are also two high YS samples from Block 2 corresponding to H ≈ 10 mm and YS = 914.5 MPa (Fig. 6c) and H ≈ 4 mm, YS = 915.6 MPa (Fig. 6d). The overall average porosity for the measured volume of the specimens was measured to be 0.104 % for the low YS specimens, and 0.062 % for the high YS specimens. Note that these porosity measurements are not wholly representative of the average porosity of the entire specimen or gauge length, as the pores are randomly distributed and their measurements may be affected by the sampling.

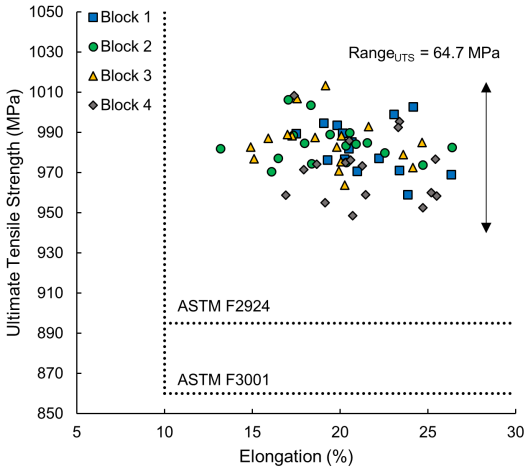

Figure 3: Scatter plot of the UTS compared to the elongation for each of the 68 tests. The data points are color coded to correspond to each block. Dotted lines represent the minimum UTS and elongation requirements for both ASTM F3001-14 [12] and ASTM F2924-14 [13].

3.3. Microstructure

In order to analyze the texture of the as-built material and rule out any texture effects contributing to tensile property variation, Fig. 7a–d shows representative EBSD inverse pole figure (IPF) maps from each of the four blocks and build plate locations. All maps and pole figures are parallel to the build direction. The pole figure heat-maps that are present at the bottom corner of each IPF map have been normalized to the highest intensity measured for the four specimens, and are taken from the regions of interest (ROI) IPF maps shown in Fig. 7. The crystallographic orientation for the blocks show similar $< 11\bar{2}0 >_{\alpha}$ texture for all four blocks.

The α-lath thickness was measured from the BSE images of the flat and polished fractured tensile specimens that are presented in Fig. 8. The three images presented are for the same specimens shown from fractography in Fig. 5, and are of the lowest YS (Fig. 8a – 859.3 MPa, Z = 25 mm, α-lath = 0.49 µm ± 0.14 µm), medium YS (Fig. 8b – 898.5 MPa, Z = 14 mm, α-lath = 0.47 µm ± 0.10 µm), and highest YS specimen (Fig. 8c – 933.6 MPa, Z = 2 mm, α-lath = 0.37 µm ± 0.10 µm). The α-lath morphology of the specimens shown in Fig. 8 is of α/β Widmänstatten, also known as basket weave acicular microstructure, typical of PBF-EB Ti-6Al-4V.

In order to quantify α-lath thickness with respect to build height, the α-laths were measured in each field of view (FOV) for several specimens at different build heights, and are presented in Fig. 9. The error bars represent 1σ for 50 α-lath measurements at each FOV. The thickness of the α-laths does not substantially increase as build height increases.

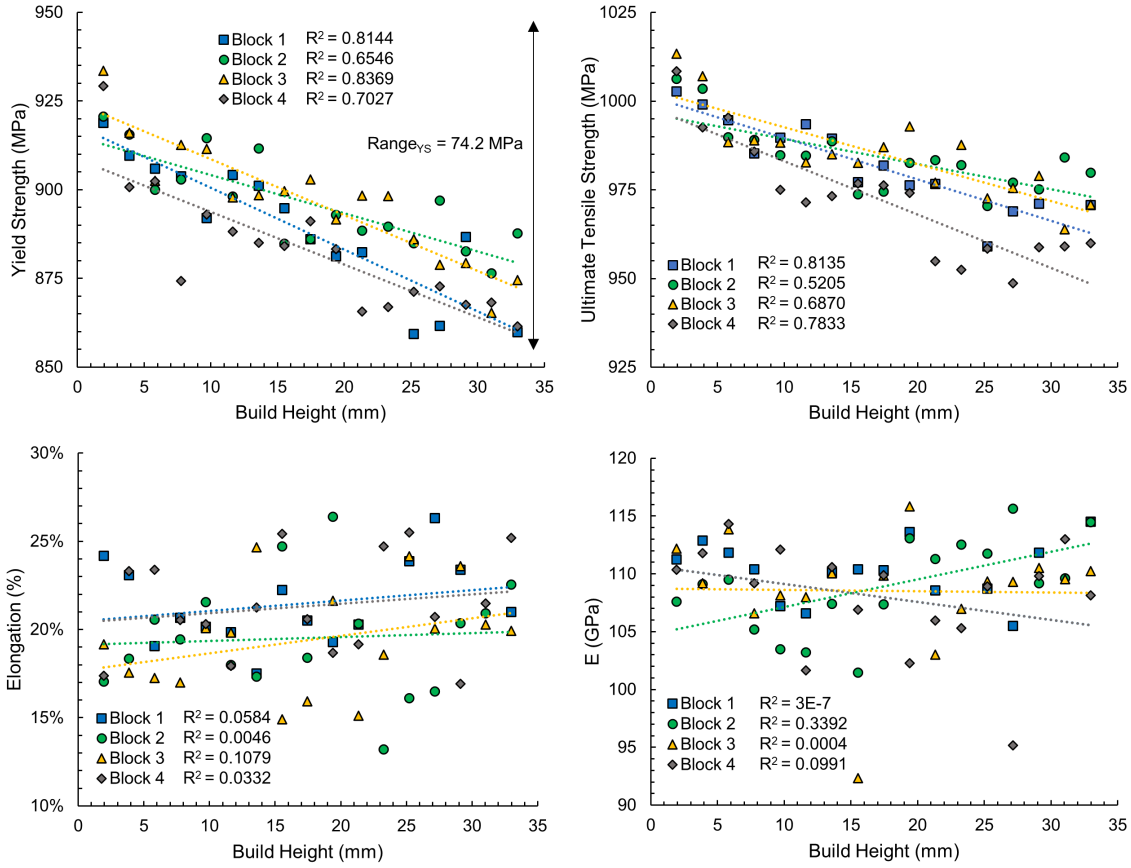

Figure 4: All tensile properties with respect to build height. R^2 values are presented with the data legend for each linear regression. Note, the linear regressions for elongation and modulus are presented, however with low R^2 values simply to illustrate that there is no trend with respect to build height.

Fig. 10 plots the α-lath size with respect to the measured YS of that particular specimen. The black thin and thick dotted lines are trends of from Tiley et al. [26] and Kar et al. [27] for YS versus α-lath thickness, and will be discussed later.

3.4. Chemistry

Inert gas fusion oxygen results are presented side by side with yield strength values for Block 4 in Fig. 11. Linear regression trendlines are presented as dotted lines through the data points. These measurements include material coming from the grip/filet section all the way to the fractured surface of the mini tensile specimens. The oxygen chemistry data presented in Fig. 11 displays the same trend as YS (oxygen decreasing with increasing build height), albeit with more scatter when compared to the YS measurements of the same block.

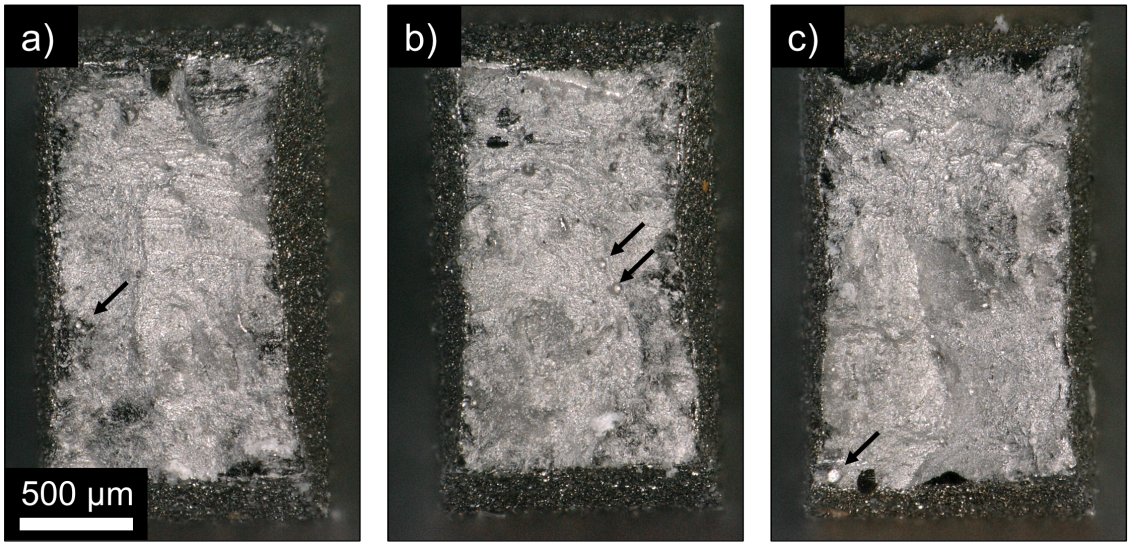

Figure 5: Representative optical fractographs of a) low yield strength specimen (859.3 MPa), b) medium yield strength specimen (898.5 MPa), and c) high yield strength (933.6 MPa). Black arrows indicate pores present on the fracture surface.

4. Discussion

From Fig. 4, it is clear that YS/UTS decreases with increasing build height. There is no observable effect of build plate location, as all blocks, in all four corners of the build plate, display the same trend as well as approximate magnitude and range of YS/UTS. The range (Range_{YS}) of YS values was equal to 74.2 MPa, which when viewed in the context of where the specimens were extracted from the material with respect to build height in Fig. 4, could be an effect attributable to the Z-location in the build, but cannot reasonably be described by build location when considering the spread of results within each build plate location, and the overall similarity of the four build plate locations measured. In order to understand the cause(s) of this observed variation in YS, contributions from porosity, microstructure, and oxygen content were investigated to elucidate any effects on the tensile properties.

From Figs. 5 and 6, porosity was not observed to correlate to YS, and therefore is unlikely to have caused the YS variation with build height observed in this work. Fractography of the specimens at the fractured gauge section surface did not reveal any significant differences between low, medium, or high YS specimens. While there are small surface pores present on most of the fractured surfaces, it is not likely these contributed to the 74.2 MPa overall variation. The solid volume fraction for two low YS specimens was measured by µXCT in the gauge section volume to be 99.8957 %, while the solid volume fraction for two high YS specimens were 99.9377 %. This small change in porosity is unlikely to have caused the observed change in YS. These values are likely to be an overestimation of the actual porosity levels in the bulk, since

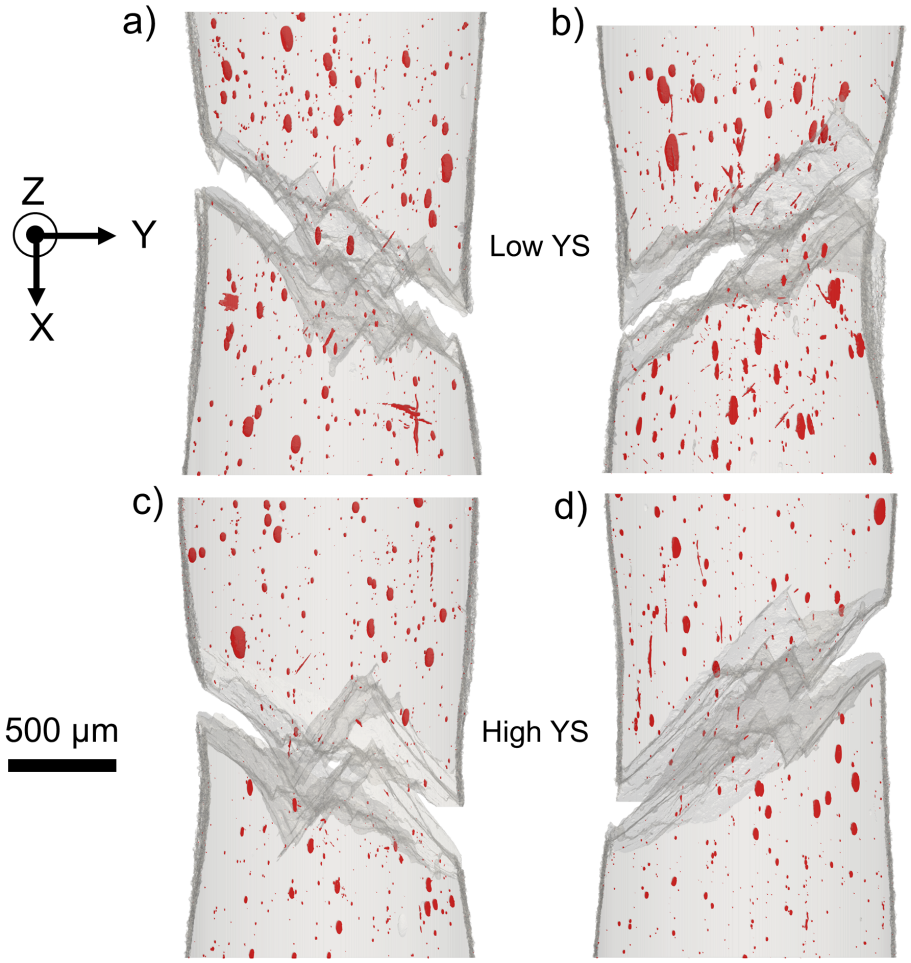

Figure 6: µXCT 3D reconstructions of the fractured specimens, displaying internal porosity highlighted in red and the exterior air/metal interface in translucent gray. a) Block 1, height (H) ≈ 33 mm, YS = 859.0 MPa b) Block 1, H ≈ 27 mm, 861.6 MPa c) Block 2, H ≈ 10 mm, YS = 914.5 MPa d) Block 2, H ≈ 4 mm, YS = 915.6 MPa.

elongated pores in the necked region were included in these measurements. This has been previously shown to occur in AM materials containing porosity after tensile deformation [28].

Shanbhag et al. [18] support this conclusion, as they also found little correlation between strength and porosity for these range of values in PBF-EB Ti-6Al-4V. A study by Watring et al. [29] in PBF-L Inconel 718 showed that for porosity levels of 0.07 vol.% and 0.23 vol.%, no difference in UTS was measured. There was a small difference in observed YS, but this difference was ultimately attributed to the effective grain size along the loading axis. Furthermore, in the aforementioned Shanbag study, porosity at levels similar to those observed in this work (for horizontally oriented tensile directions) mostly had an effect on necking and total elongation, while strength remained relatively unaffected.

The crystallographic texture was measured via EBSD from a representative piece for each of the rect-

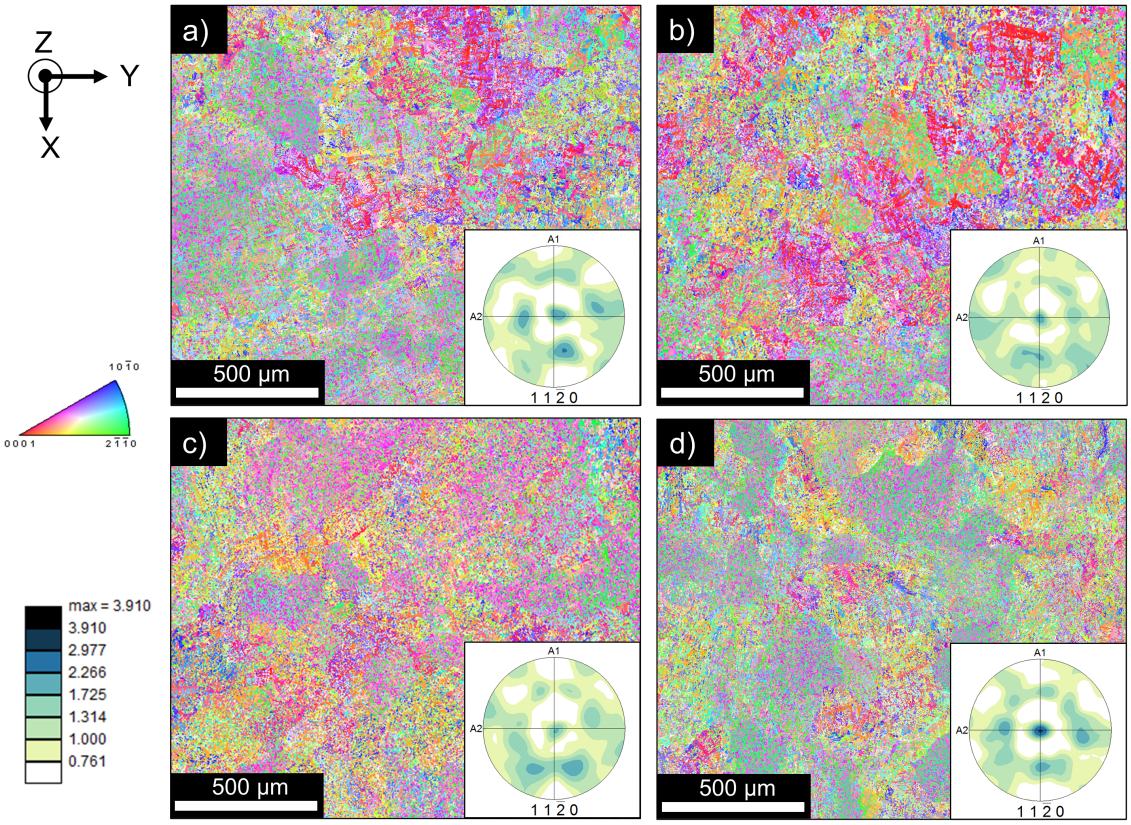

Figure 7: Representative EBSD IPF maps of each of the four blocks on the build plate. a) Block 1, b) Block 2, c) Block 3, and d) Block 4. Pole figures for the ROI are presented with each IPF map. The rainbow IPF map color legend indicates direction of the crystal by color, whereas the color bar shaded white to dark blue indicates intensity for the pole figures.

angular as-built blocks (each corner of the build plate). The crystallographic texture for all four regions showed the same relatively weak texture character in the $11\bar{2}0$ direction. Previous work on PBF-EB Ti-6Al-4V by Saville et al. [30] demonstrates that for samples containing relatively weak texture, there is little to no dependence of texture on build height. Thus, it is reasonable to assume that each block across the entire build height in this work contained the same similarly weak texture. Given this, the texture differences can be ruled out as a contributing factor to any potential differences between the blocks. From Fig. 7, EBSD was not found to vary for any of the locations in this build and so is unlikely to have caused the observed YS variation with build height. The authors note that while variations in dislocation density, variant selection, and twin density can affect the mechanical properties of the material in localized regions, it is unlikely that these were affected by the build height, particularly in PBF-EB built materials, which has a high background temperature and lower solidification and cooling rates than laser-based methods. Although thermally induced twinning has been observed by Zhong et al. [31] in laser metal deposition of Ti-6Al-4V, the cooling rate and thermal histories in the present work are going to be different as the PBF-EB process is maintained

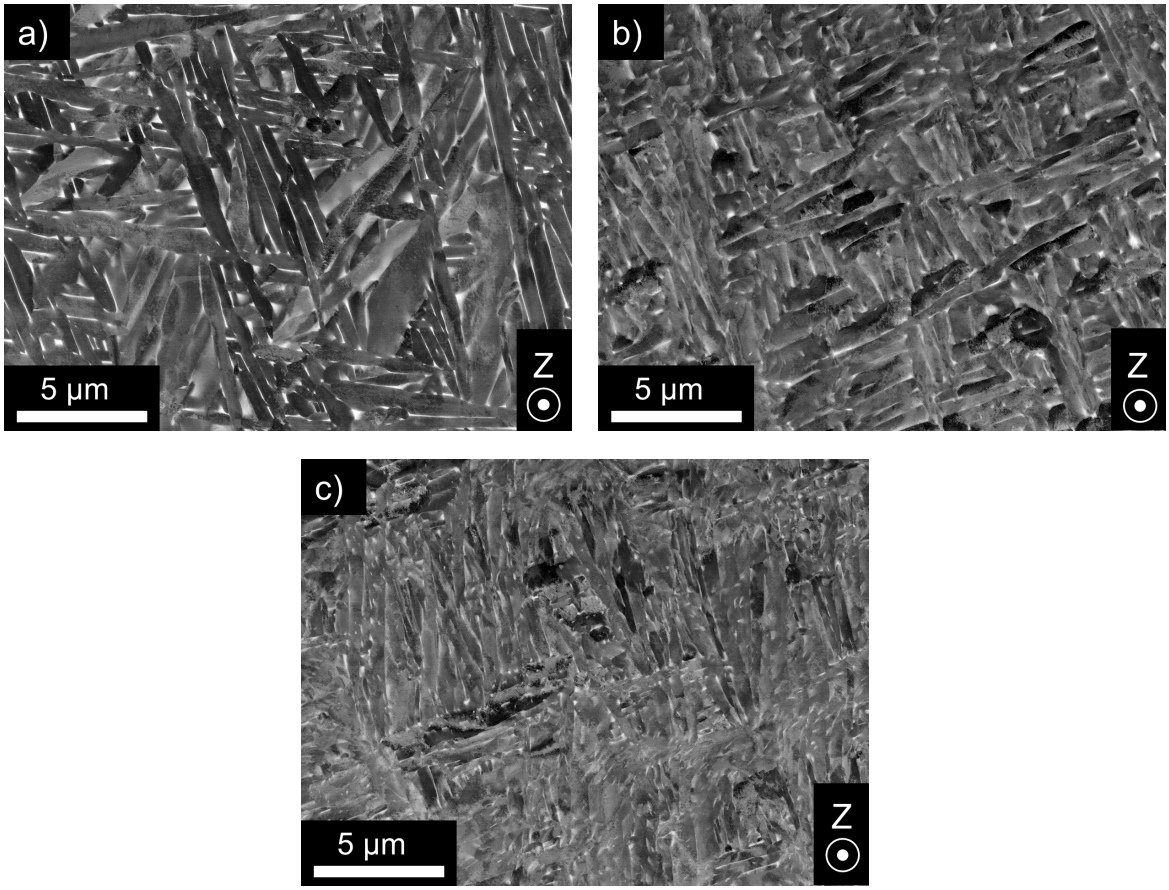

Figure 8: Representative BSE images of a) low yield strength specimen (859.3 MPa), b) medium yield strength specimen (898.5 MPa), and c) high yield strength (933.6 MPa).

around 600 °C to 800 °C.

The microstructures of the lowest YS specimen (859.3 MPa), a medium YS specimen (898.5 MPa), and highest YS specimen (933.6 MPa) were investigated via BSE imaging. The α/β Widmänstatten microstructure was observed in each of the specimens. Ghamarian et al. [32] compared empirical models for YS, and showed the contributions to YS from influential terms such as intrinsic yield strength, solid solution strengthening, Hall-Petch α-lath strengthening, and constrained β within the Widmänstatten microstructure. For α + β processed alloys, contributions to YS for Hall-Petch α-lath thickness are approximately 5 % at most for total yield strength compared to the other factors. The measured α-laths plotted in Fig. 9 show an average range of α-lath thickness of 0.37 µm – 0.53 µm with a standard deviation of all the measurements equal to ± 0.13 µm. There are enough statistically significant differences between α-lath thickness for the specimens measured in Fig. 9 ($p<0.05$, Tukey-Kramer Multiple Comparisons Test) to suggest a slight increase in α-lath thickness with increasing build height. The magnitude of the trend observed in Fig. 9 (slight increase in

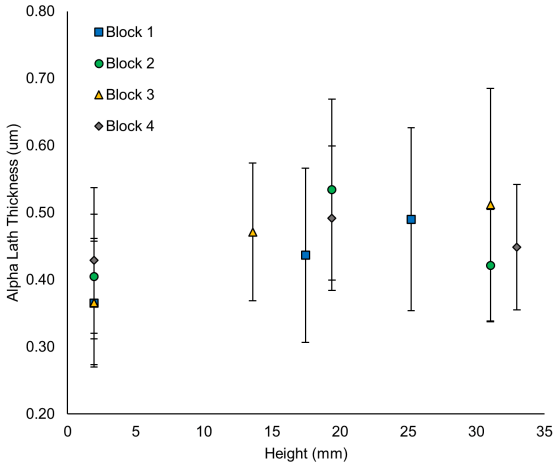

Figure 9: Plot of build height versus the measured α-lath thickness at each height. Error bars represent 1σ for 50 α-lath measurements.

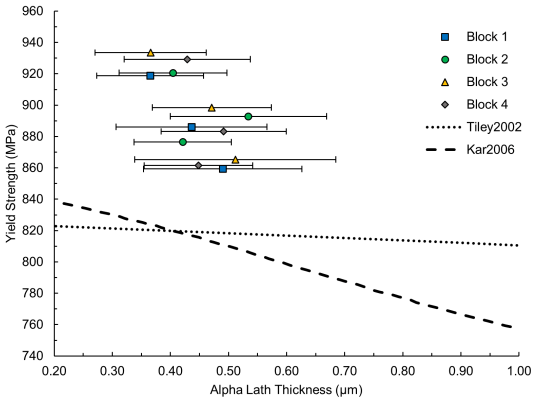

Figure 10: Plot of α-lath thickness versus yield strength. Black thin [26] and thick [27] dotted lines represent modeled yield strength as a function of α-lath thickness. Error bars represent 1σ for 50 α-lath measurements.

α-lath thickness with increasing build height) is likely too small to have any significant effect on the observed YS variation.

The average α-lath thicknesses were plotted against the corresponding YS for several specimens in Fig. 10. Work by Tiley et al. [26] and Kar et al. [27] proposed α-lath dependent models for YS, and are plotted as thin and thick black dotted lines, respectively, in Fig. 10. The entire range of YS values for the Tiley model is much tighter than that of the Kar model, however, the α-lath values obtained in the present investigation do not directly match up to either of the models for YS, as shown in Fig. 10. In the Tiley model [26], a change of approximately 75 MPa from α-lath thickness is not predicted for the ranges shown in Fig. 9. Namely, the maximum change in YS for α-lath thickness from 0.20 μm to 1.00 μm is approximately 5 MPa. If we take the Kar empirical fit into account [27], the expected change in YS from our measured values of

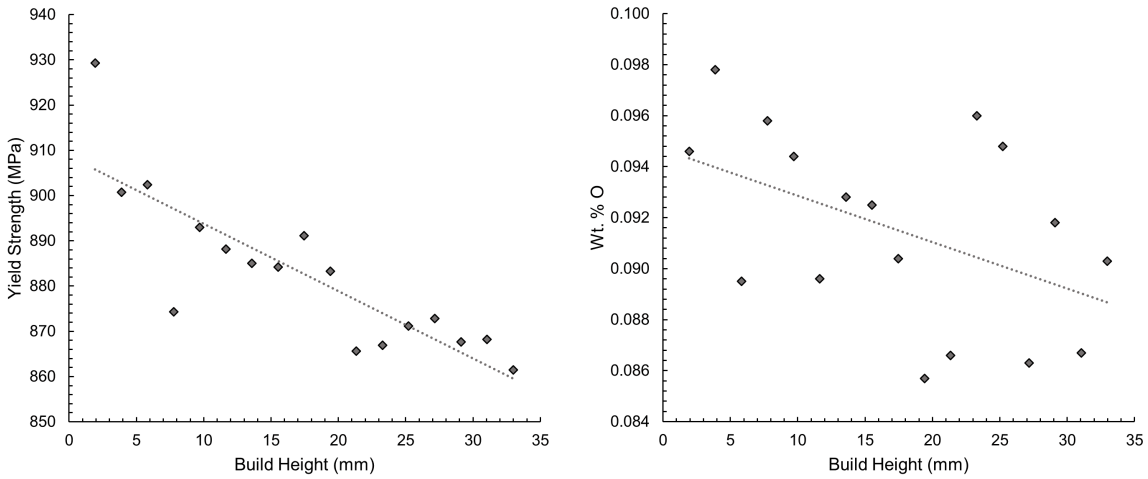

Figure 11: Scatter plots for yield strength and oxygen as a function of build height for Block 4 with dotted lines representing linear regression trendlines.

α-lath thickness would be approximately 15 MPa. If we plot the inverse square root effective diameter for the α-laths against YS to investigate Hall-Petch correlations between the blocks, as in Fig. 12, the slope of the data does not correlate to a previous study done of Hall-Petch strengthening on Ti-6Al-4V with similar Widmänstatten microstructure [33]. This indicates that Hall-Petch alone, assuming a continuing linear trend, cannot describe the observed change in YS. These values, paired with the observations by Ghamarian [32], indicate that the α-lath thickness for each of the specimens, while slightly different, are not likely to be solely responsible for the 75 MPa variation in YS, when plotted against build height. The β phase fraction at the top of the blocks was approximated from the BSE images to be roughly 3 % β (Fig. 8a) and the bottom to be roughly 1 % β (Fig. 8c). This amount of change in β phase fraction is also not predicted by the Ghamarian model to have a significant contribution to the YS (0 % contributions to total YS for $\alpha + \beta$ processed Ti-6Al-4V, and approximately 2.4 % overall contribution in total YS for β processed Ti-6Al-4V). The study by Ghamarian suggests that the main contributing factor to YS is solid solution strengthening [32].

As shown in Fig. 11, oxygen content decreases with increasing build height, and because this is the same trend observed for YS, this suggests oxygen content may be the main cause of the observed YS variation in this work. The sintered powder from the build plate for this work was previously studied by Derimow et al. [16], where it was established that there is a build height dependence for oxidation in the sintered powder bed. That is, the bottom powder layers are more rich in oxygen than powder sampled towards the top of the powder bed. There is a downward trend of oxidation back to nominal oxygen levels in the powder batch.

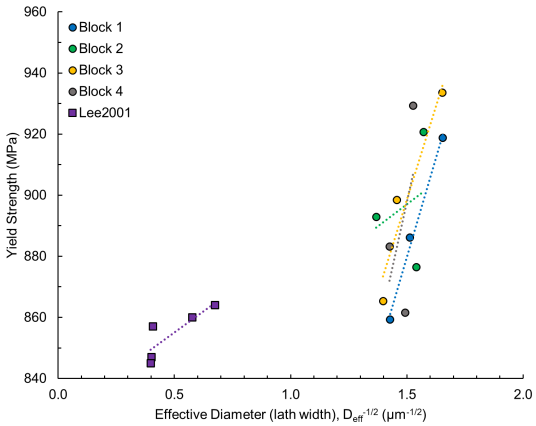

Figure 12: Plot of α-lath thickness represented as an inverse, square root effective diameter, $D^{-1/2}$ versus yield strength. Purple data markers represent data from Ref. [33].

When the powder from the top 3 mm and bottom 3 mm of the powder bed were compared directly for several powder samplings, there was a consistent difference in oxygen content, such that the top of the powder bed contained less oxygen than the bottom. This indicated that the bottom layers had scrubbed the atmosphere in the build chamber via the high background processing temperature and/or layer preheating for the PBF-EB process. The inert gas fusion oxygen tests carried out in this work for Block 4 at each height show a similar downward trending oxygen content as build height increases. It is possible that oxygen is not the sole contributing factor to this build height dependency. Within the context of solid solution strengthening, Ghamarian et al. [32] show the two largest contributors are oxygen and aluminum content. The Al wt.% values within the range of ASTM F3001-14 [12] of $5.5 < x < 6.5$ account for approximately 45 MPa in YS change according to both phenomenological models used therein. The oxygen contributions to YS variation from 0.08 wt.% O up to the ASTM F3001-14 limit of 0.13 wt.% O were modeled to be approximately 60 MPa in Ref. [32]. There may be an interplay of both Al and O changing as a function of build height in the specimens studied in this work. However, effects due to Al content, as well as other elements, are an open area of investigation. The effects of energy input on Al vaporization in PBF-EB Ti-6Al-4V have been studied by Juechter et al. [34] where it was found that Al evaporation loss is greater with increasing line energy. Given that the geometry of the blocks in this build were simple rectangular cuboids, it is likely that the Al vaporization was constant on a per layer basis, and not height dependent. The oxygen trends in this work may be one piece of the puzzle towards understanding the YS build height dependence in Ti-6Al-4V produced by PBF-EB, and results of oxygen testing are at least in agreement with previous trends of build height-influenced oxygen differences in the sintered powder [16] and top surfaces in as-built material [35].

Given that the sintered powder capsules used in Ref. [16] were adjacent to the as-built material studied in this present work, it is not unreasonable to posit that a similar trend in oxygen content with respect to build height was similarly observed herein.

This newly observed oxygen content decrease, and corresponding YS decrease, with increasing build height can be used to further optimize the PBF-EB Ti-6Al-4V process as recovered powder will have a variation in oxygen along the build height [16]. Potential improvements will be discussed in more detail in Part 2 of this work.

5. Conclusions

Four rectangular cuboid blocks of PBF-EB Ti-6Al-4V were built from virgin Grade 23 ELI powder in order to extract 68 mini tensile specimens (17 per block) for tensile testing. These as-built specimens were then studied via tensile testing, scanning electron microscopy, μXCT, and inert gas fusion to investigate potential intra-build variations in tensile properties, oxygen content, microstructure, and porosity, as well as discover possible correlations between the yield strength and material structure.

- There was a measured 74.2 MPa range in yield strength across all 68 tensile tests performed on the virgin, as-built Ti-6Al-4V.
- Yield strength was clearly influenced by build height from 0 mm to 35 mm, corresponding to the observed 74.2 MPa range in values from 933.6 MPa at the bottom of the build plate (2 mm Z-height) to 859.3 MPa towards the top of the powder bed (33 mm Z-height).
- We did not observe significant correlations between the observed YS variation and build plate location, porosity, α-lath thickness, or crystallographic texture.
- There was an observed downward trend of oxygen content as build height increases suggesting oxygen content variation may be a contributing factor to the observed YS variation with build height. This is in agreement with previous studies on sintered Ti-6Al-4V powder bed oxidation, owing to the yield strength differences to solid solution strengthening. There may be additional variations in solid solution strengthening elements such as Al, V, and N contributing to this effect, and will be the subject of future studies.

The newly observed dependence of YS on oxygen content as a function of build height can be used to further improve PBF-EB Ti-6Al-4V processing, which could involve active atmospheric gettering or improved

powder mixing and handling methodologies. As 3D printing technology advances towards more complex geometries, it is critical to understand the mechanical properties of the material at smaller length scales, such as those studied in the present work. Bulk mechanical properties and bulk chemistry measurements may not accurately represent the possible spatial variability effects in the printed material.

6. Acknowledgments

This research was performed while N. Derimow, O. Kafka, and N. Moser held National Research Council (NRC) Postdoctoral Research Associateships at the National Institute of Standards and Technology. The authors wish to thank Sol Barraza and Julio Diaz for their assistance in the laboratory, and Skye Stuckey at 3D Systems for their help with chemical analysis. The authors would also like to thank Mahdi Habibnejad, Advanced Powder and Coatings (AP&C), and GE Additive for their powder contributions to this research. The authors also wish to thank Enrico Lucon and Jordan Weaver at NIST for their helpful feedback.

References

[1] L. C. Zhang, Y. Liu, S. Li, Y. Hao, Additive Manufacturing of Titanium Alloys by Electron Beam Melting: A Review, Advanced Engineering Materials 20 (5) (2018) 1–16. doi:10.1002/adem.201700842.

[2] S. M. Gaytan, L. E. Murr, F. Medina, E. Martinez, M. I. Lopez, R. B. Wicker, Advanced metal powder based manufacturing of complex components by electron beam melting, Materials Technology 24 (3) (2009) 180–190. doi:10.1179/106678509X12475882446133.

[3] L. E. Murr, E. V. Esquivel, S. A. Quinones, S. M. Gaytan, M. I. Lopez, E. Y. Martinez, F. Medina, D. H. Hernandez, E. Martinez, J. L. Martinez, S. W. Stafford, D. K. Brown, T. Hoppe, W. Meyers, U. Lindhe, R. B. Wicker, Microstructures and mechanical properties of electron beam-rapid manufactured Ti-6Al-4V biomedical prototypes compared to wrought Ti-6Al-4V, Materials Characterization 60 (2) (2009) 96–105. doi:10.1016/j.matchar.2008.07.006.
URL http://dx.doi.org/10.1016/j.matchar.2008.07.006

[4] N. Hrabe, N. Barbosa, S. Daniewicz, N. Shamsaei, Findings from the NIST/ASTM Workshop on Mechanical Behavior of Additive Manufacturing Components, NIST Advanced Manufacturing Series (2016). doi:https://doi.org/10.6028/NIST.AMS.100-4.

[5] M. Qian, W. Xu, M. Brandt, H. Tang, Additive manufacturing and postprocessing of Ti-6Al-4V for superior mechanical properties, MRS Bulletin 41 (10) (2016) 775–784. doi:10.1557/mrs.2016.215.

[6] N. Hrabe, T. Quinn, Effects of processing on microstructure and mechanical properties of a titanium alloy (Ti-6Al-4V) fabricated using electron beam melting (EBM), part 1: Distance from build plate and part size, Materials Science and Engineering A 573 (2013) 264–270. doi:10.1016/j.msea.2013.02.064.
URL http://dx.doi.org/10.1016/j.msea.2013.02.064

[7] N. Hrabe, T. Quinn, Effects of processing on microstructure and mechanical properties of a titanium alloy (Ti-6Al-4V) fabricated using electron beam melting (EBM), Part 2: Energy input, orientation, and location, Materials Science and

Engineering A 573 (2013) 271–277. doi:10.1016/j.msea.2013.02.065.
URL http://dx.doi.org/10.1016/j.msea.2013.02.065

[8] H. P. Tang, M. Qian, N. Liu, X. Z. Zhang, G. Y. Yang, J. Wang, Effect of Powder Reuse Times on Additive Manufacturing of Ti-6Al-4V by Selective Electron Beam Melting, Jom 67 (3) (2015) 555–563. doi:10.1007/s11837-015-1300-4.

[9] H. Galarraga, D. A. Lados, R. R. Dehoff, M. M. Kirka, P. Nandwana, Effects of the microstructure and porosity on properties of Ti-6Al-4V ELI alloy fabricated by electron beam melting (EBM), Additive Manufacturing 10 (2016) 47–57. doi:10.1016/j.addma.2016.02.003.
URL http://dx.doi.org/10.1016/j.addma.2016.02.003

[10] M. Kahlin, H. Ansell, J. J. Moverare, Fatigue behaviour of notched additive manufactured Ti6Al4V with as-built surfaces, International Journal of Fatigue 101 (2017) 51–60. doi:10.1016/j.ijfatigue.2017.04.009.
URL http://dx.doi.org/10.1016/j.ijfatigue.2017.04.009

[11] N. Derimow, N. Hrabe, Oxidation in Reused Powder Bed Fusion Additive Manufacturing Ti-6Al-4V Feedstock: A Brief Review, Jom 73 (11) (2021) 3618–3638. doi:10.1007/s11837-021-04872-y.
URL https://doi.org/10.1007/s11837-021-04872-y

[12] ASTM F3001-14, Stanrdard Specification for Additive Manufacturng Titanium-6 Aluminum-4 Vanadium ELI (Extra Low Interstitial) with Powder Bed Fusion, ASTM Standards (2014) 1–6doi:10.1520/F3001-14.

[13] ASTM F2924-14, Standard Specification for Additive Manufacturing Titanium-6 Aluminum-4 Vanadium with Powder Bed Fusion, ASTM Standards (2014). doi:10.1520/F2924-14.2.

[14] V. V. Popov, A. Katz-Demyanetz, A. Garkun, M. Bamberger, The effect of powder recycling on the mechanical properties and microstructure of electron beam melted Ti-6Al-4V specimens, Additive Manufacturing 22 (June) (2018) 834–843. doi:10.1016/j.addma.2018.06.003.
URL https://doi.org/10.1016/j.addma.2018.06.003

[15] D. Coney, M. Lasker, Aerospace Structural Metals Handbook, Code 3801, 1969.

[16] N. Derimow, A. Romero, A. Rubio, C. Terrazas, F. Medina, R. Wicker, N. Hrabe, Sintered powder oxidation variation as a function of build height for titanium alloy produced by electron beam powder-bed fusion, Additive Manufacturing Letters 1 (2021) 100023. doi:10.1016/j.addlet.2021.100023.
URL https://doi.org/10.1016/j.addlet.2021.100023

[17] V. L. Stout, M. D. Gibbons, Gettering of gas by titanium, Journal of Applied Physics 26 (12) (1955) 1488–1492. doi:10.1063/1.1721936.

[18] G. Shanbhag, E. Wheat, S. Moylan, M. Vlasea, Effect of specimen geometry and orientation on tensile properties of Ti-6Al-4V manufactured by electron beam powder bed fusion, Additive Manufacturing 48 (PA) (2021) 102366. doi:10.1016/j.addma.2021.102366.
URL https://doi.org/10.1016/j.addma.2021.102366

[19] ASTM B822-17, Standard Test Method for Particle Size Distribution of Refractory Metal Powders and Related Compounds by Light Scattering, ASTM Standards (2017). doi:10.1520/B0822-17.2.

[20] ASTM E2371-13, Standard Test Method for Analysis of Titanium and Titanium Alloys by Direct Current Plasma and Inductively Coupled Plasma Atomic Emission Spectrometry (Performance-Based Test Methodology) Coupled Plasma Atomic Emission Spectrometry (ICP-AES) 1, ASTM Standards (2013). doi:10.1520/E2371-13.2.

[21] ASTM E1409-13, Standard Test Method for Determination of Oxygen and Nitrogen in Titanium and Titanium Alloys by

Inert Gas Fusion, ASTM Standards (2013). doi:10.1520/E1409.

[22] ASTM E1447-09, Standard Test Method for Determination of Hydrogen in Titanium and Titanium Alloys by Inert Gas Fusion Thermal Conductivity / Infrared Detection, ASTM Standards ((Reapproved 2016)) (2009). doi:10.1520/E1447-09R16.2.

[23] ASTM E1941-10, Standard Test Method for Determination of Carbon in Refractory and Reactive Metals, ASTM Standards (2016). doi:10.1520/E1941-10.2.

[24] A. Du Plessis, I. Yadroitsev, I. Yadroitsava, S. G. Le Roux, X-Ray Microcomputed Tomography in Additive Manufacturing: A Review of the Current Technology and Applications, 3D Printing and Additive Manufacturing 5 (3) (2018) 227–247. doi:10.1089/3dp.2018.0060.

[25] P. J. Withers, D. Grimaldi, C. K. Hagen, E. Maire, M. Manley, A. D. Plessis, X-ray computed tomography, Nature Reviews Methods Primers 1 (18) (2021). doi:10.1038/s43586-021-00015-4.
URL http://dx.doi.org/10.1038/s43586-021-00015-4

[26] J. S. Tiley, Modeling of Microstructure Property Relationships in Ti-6Al-4V, The Ohio State University Doctoral T (2002) (2002) 192.

[27] S. Kar, T. Searles, E. Lee, G. B. Viswanathan, J. Tiley, R. Banerjee, H. L. Fraser, Modeling the tensile properties in β-processed α/β Ti alloys, Metallurgical and Materials Transactions A: Physical Metallurgy and Materials Science 37 (3) (2006) 559–566. doi:10.1007/s11661-006-0028-8.

[28] D. S. Watring, J. T. Benzing, O. L. Kafka, L. A. Liew, N. H. Moser, J. Erickson, N. Hrabe, A. D. Spear, Evaluation of a modified void descriptor function to uniquely characterize pore networks and predict fracture-related properties in additively manufactured metals, Acta Materialia 223 (2022) 117464. doi:10.1016/j.actamat.2021.117464.
URL https://doi.org/10.1016/j.actamat.2021.117464

[29] D. S. Watring, J. T. Benzing, N. Hrabe, A. D. Spear, Effects of laser-energy density and build orientation on the structure–property relationships in as-built Inconel 718 manufactured by laser powder bed fusion, Additive Manufacturing 36 (June) (2020) 101425. doi:10.1016/j.addma.2020.101425.
URL https://doi.org/10.1016/j.addma.2020.101425

[30] A. I. Saville, S. C. Vogel, A. Creuziger, J. T. Benzing, A. L. Pilchak, P. Nandwana, J. Klemm-Toole, K. D. Clarke, S. L. Semiatin, A. J. Clarke, Texture evolution as a function of scan strategy and build height in electron beam melted Ti-6Al-4V, Additive Manufacturing 46 (June) (2021) 102118. doi:10.1016/j.addma.2021.102118.
URL https://doi.org/10.1016/j.addma.2021.102118

[31] H. Z. Zhong, X. Y. Zhang, S. X. Wang, J. F. Gu, Examination of the twinning activity in additively manufactured Ti-6Al-4V, Materials and Design 144 (2018) 14–24. doi:10.1016/j.matdes.2018.02.015.

[32] I. Ghamarian, B. Hayes, P. Samimi, B. A. Welk, H. L. Fraser, P. C. Collins, Developing a phenomenological equation to predict yield strength from composition and microstructure in β processed Ti-6Al-4V, Materials Science and Engineering A 660 (2016) 172–180. doi:10.1016/j.msea.2016.02.052.
URL http://dx.doi.org/10.1016/j.msea.2016.02.052

[33] D.-G. Lee, S. Lee, C. S. Lee, S. Hur, Effects of Microstructural Parameters on the Quasi-static and Dynamic Deformation Behaviors of Ti-6Al-4V Alloys with Widmanstatten Structures, J. Kor. Inst. Met. & Mater. 39 (12) (2001) 1406–1413.

[34] V. Juechter, T. Scharowsky, R. F. Singer, C. Körner, Processing window and evaporation phenomena for Ti-6Al-4V produced by selective electron beam melting, Acta Materialia 76 (2014) 252–258. doi:10.1016/j.actamat.2014.05.037.

[35] J. Karlsson, M. Norell, U. Ackelid, H. Engqvist, J. Lausmaa, Surface oxidation behavior of Ti-6Al-4V manufactured by Electron Beam Melting (EBM®), Journal of Manufacturing Processes 17 (2015) 120–126. doi:10.1016/j.jmapro.2014.08.005.
URL http://dx.doi.org/10.1016/j.jmapro.2014.08.005